Astronomy & Astrophysics manuscript no. 8306.hyper25325
March 20, 2008
© ESO 2008

The close circumstellar environment of the semi-regular S-type star π^1 Gruis⋆,⋆⋆

S. Sacuto[1,2], A. Jorissen[3], P. Cruzalèbes[1], O. Chesneau[1], K. Ohnaka[4], A. Quirrenbach[5], and B. Lopez[1]

[1] Observatoire de la Côte d'Azur, Dpt. Gemini-CNRS-UMR 6203, Avenue Copernic, F-06130 Grasse, France
[2] Department of Astronomy, University of Vienna, Türkenschanzstraße 17, 1180 Vienna, Austria
e-mail: stephane.sacuto@obs-azur.fr ; stephane.sacuto@univie.ac.at
[3] Institut d'Astronomie et d'Astrophysique, Université Libre de Bruxelles, Campus Plaine C.P. 226, Boulevard du Triomphe, B-1050 Bruxelles, Belgium
[4] Max-Planck-Institut für Radioastronomie, Auf dem Hügel 69, 53121 Bonn, Germany
[5] ZAH Landessternwarte, Koenigstuhl 12, 69117 Heidelberg, Germany

Received; accepted

ABSTRACT

Aims. We study the close circumstellar environment of the nearby S-type star π^1 Gruis using high spatial-resolution, mid-infrared observations from the ESO/VLTI.

Methods. Spectra and visibilities were obtained with the MIDI interferometer on the VLT Auxiliary Telescopes. The cool M5III giant β Gruis was used as bright primary calibrator, and a dedicated spectro-interferometric study was undertaken to determine its angular diameter accurately. The MIDI measurements were fitted with the 1D numerical radiative transfer code DUSTY to determine the dust shell parameters of π^1 Gruis. Taking into account the low spatial extension of the model in the 8-9 μm spectral band for the smallest projected baselines, we consider the possibility of a supplementary molecular shell.

Results. The MIDI visibility and phase data are mostly dominated by the spherical 21 mas (694 $R_\odot$) central star, while the extended dusty environment is over-resolved even with the shortest baselines. No obvious departure from spherical symmetry is found on the milliarcsecond scale. The spectro-interferometric observations are well-fitted by an optically thin ($\tau_{\rm dust}$<0.01 in the N band) dust shell that is located at about 14 stellar radii with a typical temperature of 700 K and composed of 70% silicate and 30% of amorphous alumina grains. An optically thin ($\tau_{\rm mol}$<0.1 in the N band) H_2O+SiO molecular shell extending from the photosphere of the star up to 4.4 stellar radii with a typical temperature of 1000 K is added to the model to improve the fit in the 8-9 μm spectral band. We discuss the probable binary origin of asymmetries as revealed by millimetric observations.

Key words. Techniques: interferometric; Techniques: high angular resolution; Stars: AGB and post-AGB; Stars: circumstellar matter; Stars: mass-loss

hal-00266023, version 1 - 20 Mar 2008

1. Introduction

The class of S stars is characterized by ZrO (and sometimes LaO) bands, in addition to the TiO bands present in cool oxygen-rich giants of spectral type M. The presence of lines from the unstable element Tc (technetium) in the spectra of intrinsic S stars indicates that they are currently evolving on the thermally-pulsing asymptotic giant granch (TP-AGB), where internal nucleosynthesis is responsible for forming carbon and heavy elements (*s-elements*) subsequently dredged up to the stellar surface. Being on the AGB, intrinsic S stars experience a mass-loss allowing the formation of their dust circumstellar environment (Jorissen & Knapp, 1998).

At a distance of 153^{+28}_{-20}pc (Perryman et al., 1997; Van Eck et al., 1998), π^1 Gruis (Hen 4-202, HD 212087, HIP 110478) is one of the brightest intrinsic S stars. It is a semi-regular variable of type SRb, varying from V=5.4 to 6.7 in 150 days. It was chosen as an original prototype of the S star class with R And and R Cyg (Merrill, 1922), and is known to be a binary star with a solar-type G0V companion, located at an angular distance of 2.71″ (unchanged for more than a century; Bonneau, priv. comm.), with a position angle of 202.1° and an apparent visual magnitude of 10.9 (Feast, 1953). The pair is probably physical with their apparent magnitude agreeing with their spectral type for the Hipparcos distance.

With C/O ratios generally around 0.8 (Smith & Lambert, 1986), photospheres of S-type stars are oxygen-rich. The situation regarding π^1 Gruis is somewhat confusing, though. According to its position in IR color-color diagrams, π^1 Gruis is classified in the C class of intrinsic S stars (Jorissen & Knapp, 1998). This class includes stars with a dense oxygen-rich circumstellar envelope and with strong chemical peculiarities and mass-loss rates ranging from a few 10^{-7} to a few 10^{-5} $M_\odot\,yr^{-1}$. Furthermore, this star is classified as E (emission silicate)

Send offprint requests to: S. Sacuto

⋆ Based on observations made with the Very Large Telescope Interferometer at Paranal Observatory under programs 077.D-0294(D/E/F)

⋆⋆ Reduced visibilities and differential phases are available in electronic form at the CDS via anonymous ftp to cdsarc.u-strasbg.fr (130.79.128.5) or via http://cdsweb.u-strasbg.fr/cgi-bin/qcat?J/A+A/?/?

by Volk & Cohen (1989) and SE (silicate and oxygen-rich dust emission) by Sloan & Price (1998). The circumstellar dusty shell of π^1 Gruis would thus appear to be mainly composed of oxygen-rich elements; however, the track in the (K-[12],[25]-[60]) color-color diagram during the variability cycle (Jorissen & Knapp, 1998) suggests that the shell emission could as well be associated with carbon-composite material (Thomas et al., 1976; Knapp et al., 1999a).

The mass-loss history of the star can be traced back 21,000 years, with the detection of a 0.28 pc extended dust shell by IRAS, assuming a 15 $\mathrm{km\,s^{-1}}$ velocity of expansion (Young et al., 1993). The molecular environment was resolved in the east-west direction with a 24″ (Sahai, 1992) and a 30″ beam (Knapp et al., 1999a). Moreover, the CO lines exhibit an unusual asymmetric double-horned profile and a high-velocity component interpreted in the frame of a slowly expanding disk and a fast ($v \geq 90$ $\mathrm{km\,s^{-1}}$) north-south bipolar outflow. Chiu et al. (2006) report millimeter observations at higher spatial resolution (2.1″×4.2″ beam) that confirm this interpretation. In addition, these observations reveal a 200 AU cavity suggesting that the mass-loss rate of π^1 Gruis has dramatically decreased over the past 90 years. Whether the highly structured far environment of π^1 Gruis (presence of disk + jet) is a consequence of the asymmetry of the dusty wind from the primary star or of the presence of the far companion, or even a closer undetected one, cannot be addressed by the millimetric observations of Chiu et al. (2006) due to insufficient spatial resolution.

Based on the comparative analysis of the jets and disks present in a sample of late AGB stars (among which V Hya and π^1 Gruis) and of proto-planetary nebulae (including symbiotic stars), Huggins (2007) strongly favors the second possibility. The properties of the disk and bipolar outflow of π^1 Gruis appear to fit nicely in a sequence going from late (binary) AGB stars to proto-planetary nebulae. According to the binary scenarios discussed by Huggins (2007), the G0V companion could be at the origin of the launching of the bipolar outflow, despite the large separation. However, Makarov & Kaplan (2005) and Frankowski et al. (2007) found possible evidence for yet another companion from the discrepancy between the Hipparcos and Tycho-2 proper motion (the Hipparcos proper motion relies on measurements spanning only 3 years, whereas the Tycho-2 one uses positional data spanning more than a century). Any discrepancy between these short-term and long-term proper motions is thus indicative of the presence of an unrecognized orbital motion in addition to the true proper motion. The discrepancy is very significant in the case of π^1 Gruis. According to the analysis of Frankowski et al. (2007), these so-called '$\Delta\mu$ binaries' correspond to systems with orbital periods in the range 1500-10^4 days, much shorter thus than the 6000-year period inferred by Knapp et al. (1999a) for the G0V companion 2.7" away. It is therefore an open question whether a third component might be present in the system.

In this paper, we present the first mid-infrared interferometric observations of this star taken with the MIDI/VLTI instrument, secured with auxiliary telescopes (ATs) of 1.8 m that provide a beam with an FWHM of 1.1″ at 10 μm. In interferometric mode, measurements of spatially correlated flux at a high spatial resolution (∼20 mas) and multi-spectral ($\lambda/\Delta\lambda$∼30) information on the mid-infrared source was obtained within the interferometric field-of-view (FOV) of 1.1″. The inner diameter of the millimetric disk (∼2.6″) found by Chiu et al. (2006) is then largely beyond the present MIDI FOV, as is the distant companion (2.71″). The outline of this paper is as follows. In Sect. 2, we present the MIDI observations and describe the calibration performed with the two data-reduction software packages (MIA and EWS) developed for the MIDI focal instrument. This calibration required considerable effort to determine the angular diameter of the spatially resolved calibrator M5III star β Gruis (described in Appendix A). Section 3 presents our spectro-photometric and interferometric interpretations of the star. This was done first with an analytical radiative transfer model which gives some insight into the expected behavior of the mid-infrared emission from the circumstellar envelope. Then, we used the numerical radiative transfer code DUSTY to confirm the set of parameters found with the analytical thin-dusty-shell model and define a chemical composition of the dust shell, taking the position of the star on the *silicate dust sequence* into account. Moreover, to account for the larger than expected spatial extension of the object in the 8-9 μm spectral band, we add a molecular shell to the model. In Sect. 4, we discuss the probable binary origin of asymmetries revealed by millimetric observations. Finally, we summarize and conclude in Sect. 5.

2. Observations and calibration process

The Very Large Telescope Interferometer (VLTI) of ESO's Paranal Observatory was used with MIDI, the MID-infrared Interferometric recombiner (Leinert et al., 2003). MIDI combines the light of two telescopes and provides spectrally resolved visibilities in the N band atmospheric window. Guaranteed time observations (GTO) of π^1 Gruis were conducted with the VLT ATs positioned at stations A0, E0, D0, and G0, providing baselines in the range of 15-64 meters. Observations were made during the nights of May 21-23-24-25-27 2006, June 19, 2006, and August 8, 2006, under good atmospheric conditions (average seeing=0.94″), with the worst seeing (=1.51″) during the night of May 27, 2006. Table 1 presents the journal of the interferometric observations. The calibrator β Gruis was either observed right before or after each science target observation.

Chopped acquisition images were recorded (f=2Hz, 2000 frames, 4 ms per frame, 98mas per pixel) for the fine acquisition of the target. The acquisition filter was an N-band filter. Simultaneous interferometric and photometric measurements were performed with the SCI-PHOT mode of MIDI, using the prism that provides a spectral dispersion of about 30. The data-reduction software packages[1] MIA and EWS (Jaffe, 2004) were used to reduce the spectra and visibilities (Chesneau et al., 2005). MIA is based on the power spectrum analysis and uses a fast Fourier transformation (FFT) to calculate the Fourier amplitude of the fringe packets, while EWS uses a shift-and-add algorithm in the complex plane, averaging appropriately modified in-

[1] `http://www.mpia-hd.mpg.de/MIDISOFT/`, `http://www.strw.leidenuniv.nl/~nevec/MIDI/`

Table 1. Journal of observations.

Star	UT date & Time	ϕ^*	Config.	B [m]	PA [deg]
π^1 Gruis	2006-05-21 09:09:26	...	E0-G0	15.7	50
β Gruis	2006-05-21 09:28:33	0.23	-	-	-
π^1 Gruis	2006-05-23 09:32:27	...	A0-G0	63.5	56
β Gruis	2006-05-23 10:06:51	0.28	-	-	-
π^1 Gruis	2006-05-24 09:27:34	...	D0-G0	31.8	56
β Gruis	2006-05-24 09:44:39	0.31	-	-	-
π^1 Gruis	2006-05-25 08:09:13	...	A0-G0	61.2	41
β Gruis	2006-05-25 07:51:28	0.34	-	-	-
π^1 Gruis	2006-05-27 09:20:41	...	E0-G0	15.9	57
β Gruis	2006-05-27 09:37:11	0.39	-	-	-
π^1 Gruis	2006-06-19 10:16:01	...	D0-G0	30.6	83
β Gruis	2006-06-19 09:50:14	0.01	-	-	-
π^1 Gruis	2006-08-08 08:40:43	...	A0-G0	52.6	102
β Gruis	2006-08-08 08:13:56	0.36	-	-	-

$*$: the pulsation phase for β Gruis (Otero & Moon, 2006). This was not possible for π^1 Gruis due to the non-regular character of its lightcurve.

dividual exposures (dispersed channeled spectra) to obtain the complex visibility.

An extensive study of the fluctuations of the instrumental transfer function was carried out for the baseline A0-G0 during the night of 2006 May 25 (see Table A.1). The rms scatter of these calibration measurements is ∼0.05 between 8 μm and 13 μm, corresponding to a relative error of 10%. This error in SCI-PHOT mode with ATs is greater than the typical errors encountered with UTs with the same observing mode (2-5%). This discrepancy is mostly due to the limited accuracy of the photometric extraction with ATs versus UTs.

All visibility and differential phase data as well as all the characteristics of the observations are available from the CDS (Centre de Données astronomiques de Strasbourg); all data products are stored in the FITS-based, optical interferometry data exchange format (OI-FITS) described in Pauls et al. (2005).

2.1. General description

Due to its proximity (153 pc) and its brightness (about 900 Jy at 10 μm), π^1 Gruis is an ideal mid-infrared target for interferometric measurements with the ATs. Interferometric observations provide the visibility measurements of the source $\widetilde{V}_{\rm sou}$, which is the product of the source calibrated visibilities $V_{\rm sou}$ with the system response $V_{\rm sys}$, which in turn is a combination of the atmospheric and instrumental responses. The system response is estimated using the ratio between visibility measurements of the calibrator $\widetilde{V}_{\rm cal}$ and its theoretical visibilities $V_{\rm cal}$ (Van Belle & Van Belle, 2005). The expression of the source calibrated visibility is

$$V_{\rm sou} = \frac{\widetilde{V}_{\rm sou}}{\widetilde{V}_{\rm cal}} V_{\rm cal}. \quad (1)$$

If the calibrator is unresolved, its theoretical visibility is close to 1 and the measured contrast of the fringes is a direct measure of the instrumental efficiency. If the calibrator is resolved, then the values of its theoretical spectrally dispersed visibilities need to be very accurately determined.

For our observations of π^1 Gruis, which has no nearby unresolved calibrator with enough flux (>100 Jy at 12 μm, corresponding to the sensitivity of MIDI with ATs in low spectral resolution and SCI-PHOT mode), two choices were possible: either move the telescope far from π^1 Gruis to acquire a bright enough unresolved calibration star or to observe a bright but resolved calibrator in the vicinity of π^1 Gruis. The first choice introduces a bias due to the air mass difference between the source observation at a given sky location and the calibrator observation at another location. The second choice requires an accurate knowledge of the angular diameter of the resolved target. The second option was chosen for optimizing the flux at the price of a potentially large uncertainty on the angular diameter of the calibration star (see Appendix A).

2.2. Calibrated flux of the source

The MIDI flux of π^1 Gruis was scaled to the MARCS model flux of β Gruis, for which we take into account the value of the diameter from the spectrometric method (26.8±1.3 mas; see Appendix A.1)

$$F_{\rm sou} = \frac{\widetilde{F}_{\rm sou}}{\widetilde{F}_{\rm cal}} F_{\rm cal}^{\rm marcs}, \quad (2)$$

where $F_{\rm sou}$ is the calibrated flux of π^1 Gruis, $\widetilde{F}_{\rm sou}$ the raw flux measurements of π^1 Gruis, $\widetilde{F}_{\rm cal}$ the raw flux measurements of β Gruis, and $F_{\rm cal}^{\rm marcs}$ the MARCS synthetic flux of β Gruis.

Figure 1 compares the single-dish MIDI spectrum with the ISO spectrum (Sloan et al., 2003) taken on 1996 Oct 26. Error bars are related to the uncertainty on the value of the calibrator diameter. The MIDI flux level is lower than the ISO/SWS flux level. Two possibilities could account for this difference. The most probable one is that the beam of an AT (∼1.1″ at 10 μm) is small compared to that of the ISO/SWS satellite (14″×22″). Therefore, because of the proximity of this star (153 pc) and the large extension of its dust envelope beyond the AT beam size, some flux might be missed. A second possibility that cannot be excluded is that the level of emission has changed since the ISO observation (1996) due to the pulsation of the star. However, this star is a semi-regular SRb pulsator with a low variability, for which it is difficult to assign a phase to a given observation. Nevertheless, we can see that the shape of the ISO/SWS and MIDI spectra is about the same, revealing a dust feature that will be discussed in Sect. 3.4.2. As a consequence, we assume in the following study that the MIDI spectrum can be complemented with the ISO spectrum to construct the current SED of the object at longer infrared wavelengths.

2.3. Calibrated visibilities of the source

In Fig. 2 are shown simultaneously the calibrated visibility with the MIA and EWS reduction softwares. The curves from the two softwares are almost indistinguishable. For clarity, we only show the reduction taking the spectrometric diameter of β Gruis into account (26.8±1.3 mas; see Appendix A.1). The error bars are the sum of the transfer function error bar of 10% plus the error bar related to the uncertainty on the value of the calibrator diameter (from 0.6% at low spatial frequencies to 10% at high spatial frequencies).

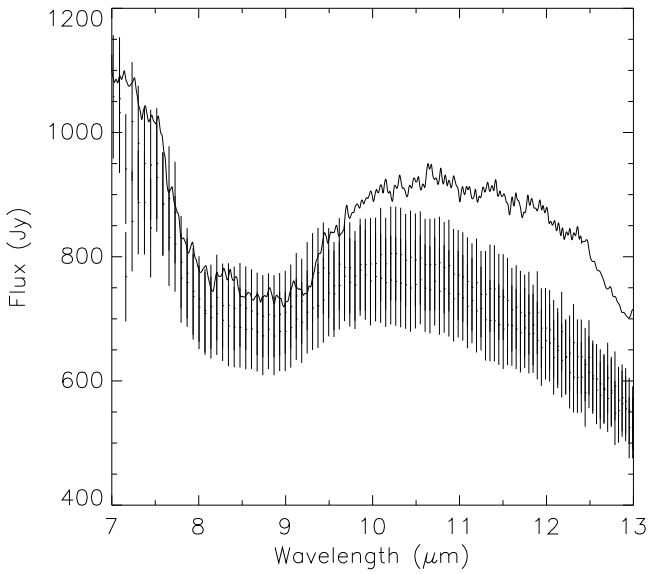

Fig. 1. Calibrated MIDI fluxes of π^1 Gruis (vertical error bars) as compared to the ISO/SWS spectrum (solid line) taken on 1996 Oct 26.

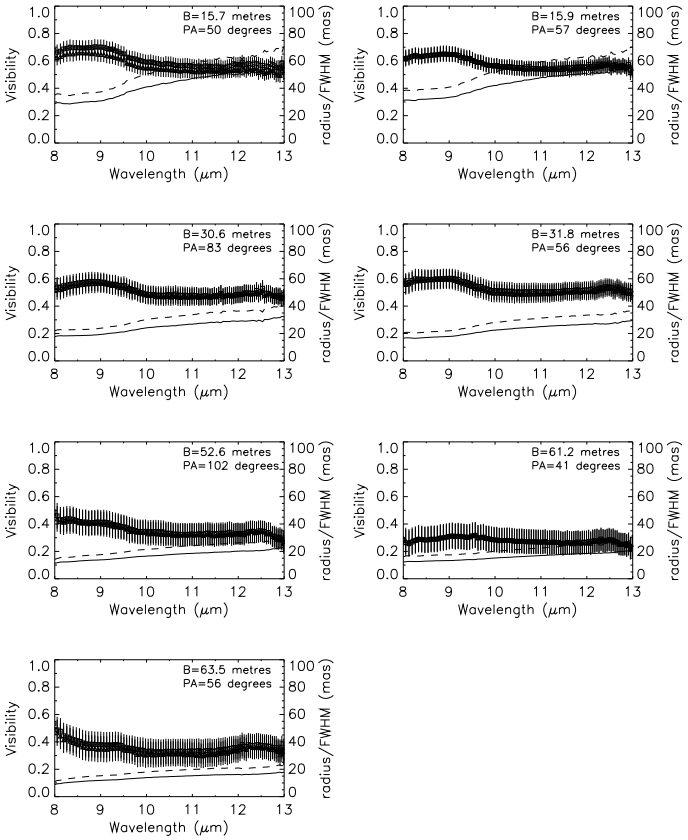

Fig. 2. MIDI-calibrated visibilities (error bars) with the MIA (squares) and EWS (triangles) reduction softwares. The solid lines correspond to the uniform disk angular radius (in mas) and the dashed lines to the FWHM (in mas) of the Gaussian distribution (both to be read from the scale on the right axis), computed from the visibility at each spectral channel.

The size derived from the uniform disk and the Gaussian distribution regularly increases from 8 to 13 μm (see Fig. 2), indicating that an extended mid-infrared structure surrounds the central star (Ohnaka et al., 2005). The dimension of this structure depends on the observed wavelength, so neither of the two simple models (monochromatic uniform-disk or Gaussian distribution) can describe the source. In the following, we model the visibilities with radiative transfer models taking into account the spectral dependency of the circumstellar environment of π^1 Gruis.

To check whether the object shows some asymmetries, one can use the differential phase of π^1 Gruis obtained from the EWS software. Figure 3 shows the calibrated differential phase of the object evaluated from all the determined projected baselines. Error bars correspond to the rms of the differential phase over all the projected baselines. The very low rms values of the differential phase ($\pm 1.93°$ at 8 μm, $\pm 1.10°$ at 9 μm, $\pm 1.65°$ at 10 μm, $\pm 1.82°$ at 12.5 μm) indicates that there is no obvious signature of an asymmetric source, such as binarity or a clumpy environment, for the given projected baselines.

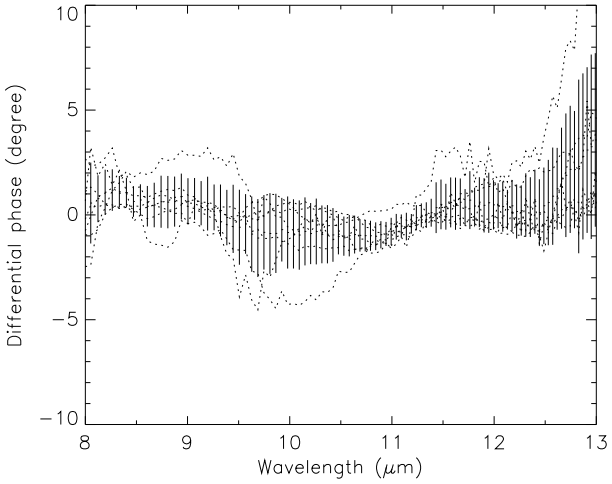

Fig. 3. Calibrated differential phase of π^1 Gruis evaluated from all the determined projected baselines (dotted lines). Error bars correspond to the rms of the differential phase averaged over all the projected baselines.

Furthermore, the MIDI visibility amplitudes also show no evident departure of the object from spherical symmetry. Figure 4 shows the dependence of the dimensions of the equivalent uniform-disk on the projected baseline position angle on the sky at different wavelengths. The three circles fit the points calculated for a given wavelength at close projected baselines for different projected baseline position angles. In addition to zero differential phase, these fits show that the object is nearly spherical. It must be pointed out that for such a close, extended giant, the interferometric fringes essentially probe the star photosphere and its close vicinity, while the extended dusty environment is over-resolved even for the shortest baselines.

From these considerations, spherical radiative transfer models will be used to interpret the spectro-interferometric data of π^1 Gruis.

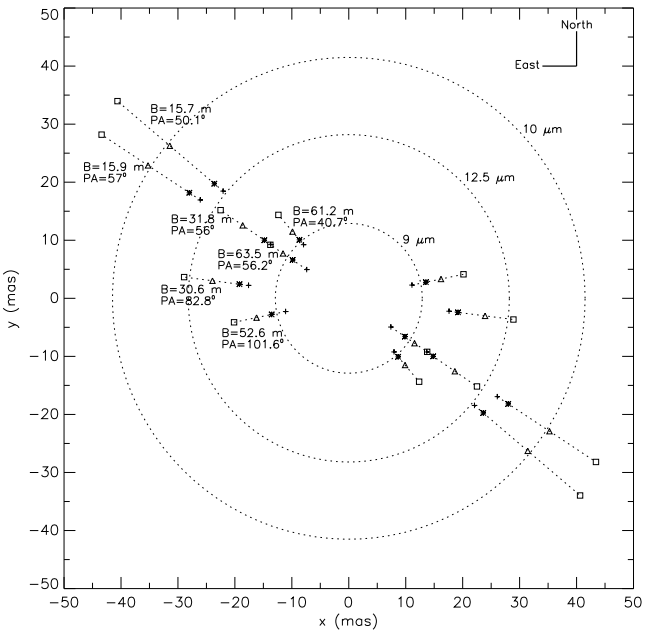

Fig. 4. This figure presents the dependence of the dimensions of the equivalent uniform-disk (in mas) on the projected baseline position angle on the sky taken at 8 (plus), 9 (cross), 10 (triangle), and 12.5 μm (square). The three dotted circles fit the points calculated for a given wavelength at close projected baselines (B) for different projected baseline position angles (PA).

3. Simultaneous fit of observed visibilities and SED

3.1. Photometric observations of π^1 Gruis

Besides the ISO/SWS spectrum (see Fig. 1), ground-based photometry is also available for π^1 Gruis (see Table 2). The K magnitude has already been dereddened by Van Eck et al. (2000b). The other magnitudes were dereddened using the Fitzpatrick absorption curve for the M-band (Fitzpatrick, 1999) and the values of Rieke & Lebofsky (1985) for the N-band. Van Eck's visual extinction value of A_v=0.17 was adopted, so that the ratio of total to selective extinction at V, 3.1 on average, allowed us to correct the other magnitudes. At wavelengths longer than 12.5 μm, the interstellar extinction becomes negligible compared to the measurement precision of the magnitude. Table 2 lists the basic photometric properties of π^1 Gruis.

3.2. The stellar atmosphere of π^1 Gruis

The realistic MARCS code (see Appendix A.1) was used to determine the synthetic intensity distribution of the S-star π^1 Gruis. Such a distribution is far more realistic than a blackbody distribution due to the large number of absorption lines in S star atmospheres.

The π^1 Gruis MARCS model atmosphere is taken from a grid specifically designed for S stars (Plez et al. (2003) and in preparation), since their non-solar C/O ratio and s-process abundances impact their atmospheric structure. Synthetic $J-K$ and $V-K$ colors were computed for all models from this grid (Fig. 5). These reveal that the C/O ratio has a strong influence on the colors, especially for low effective temperatures ($\leq$ 3200 K). There is, however, hardly a one-to-one relationship between the photometric indices and the atmospheric parameters, and several models are found to match the $(J-K)_0$, $(H-K)_0$ and $(V-K)_0$ indices of π^1 Gruis. All these models have $T_{\rm eff}$ = 3100 K, $\log g$ = 0, and [Fe/H] = 0, but allow some range in [s/Fe] and C/O (namely C/O = 0.97 for [s/Fe] = 0.5 dex, and 0.90 $\leq$ C/O $\leq$ 0.92 for [s/Fe] = 1 dex). The situation is illustrated in Fig. 5, where π^1 Gruis falls within the dashed box. It must be noted that Vanture & Wallerstein (2002) have performed a spectroscopic abundance analysis of π^1 Gruis, though not with dedicated MARCS model atmospheres, and found [Fe/H] = 0.05 ± 0.48 and [Zr/Ti] = 1.27 ± 0.23 for $T_{\rm eff}$ = 3000 K. These are in good agreement with the parameters inferred from the MARCS models. Table 3 summarizes the atmospheric parameters and the most important abundances adopted for π^1 Gruis.

Table 2. Broadband photometry of π^1 Gruis

Band	Wavelength (μm)	Extinction coefficient	Dereddened magnitude	Reference
R	0.67	0.13	3.05	(1)
I	0.87	0.09	0.45	-
H	1.65	0.03	-1.82	(2)
K	2.2	0.02	-2.07	-
L	3.6	0.01	-2.50	-
M	4.8	0.01	-2.26	-
N	8.4	0.01	-2.89	-
-	9.7	0.01	-3.25	-
-	10.5	0.01	-3.51	-
-	11.2	0.01	-3.58	-
-	12.5	0.0	-3.47	-
Q	20.0	0.0	-4.35	-
U	0.35	0.28	11.13	(3)
B	0.42	0.24	8.32	-
V	0.55	0.17	6.43	-
J	1.21	0.05	-0.60	-
H	1.66	0.03	-1.72	-
K	2.22	0.02	-2.14	-
L	3.45	0.01	-2.57	-
J	1.25	0.05	-0.71	(4)
K	2.2	0.02	-2.18	-
L	3.5	0.01	-2.51	-
M	4.9	0.01	-2.23	-
N	12.0	0.0	-3.58	-

(1) Johnson et al. (1966); (2) Thomas et al. (1976);
(3) Van Eck et al. (2000b); (4) Smith (2003)

Table 3. Stellar atmospheric parameters of π^1 Gruis, all from Vanture & Wallerstein (2002) except C/O.

Parameter	Value
$T_{\rm eff}$	3000 K
$\log g$	0.0
$v_{\rm micro}$ (km s^{-1})	3.0
$[Fe/H]$	0.05±0.48
$[Zr/Ti]$	1.27±0.23
C/O	0.97

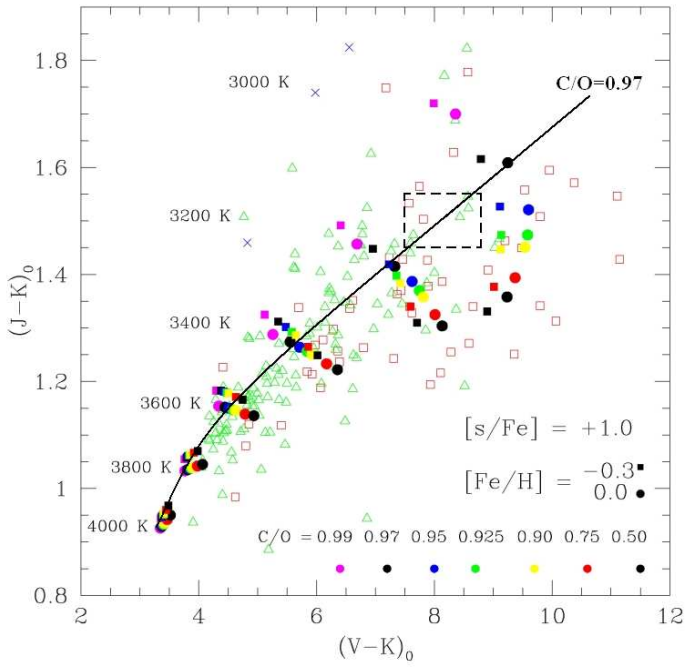

Fig. 5. Dereddened (V-K,J-K)$_0$ color-color diagram for S stars (open triangles) from Van Eck & Jorissen (2000a) and Van Eck et al. (2000b), M giants (open squares), and a few C stars (crosses) both from Whitelock et al. (2000), compared to synthetic MARCS model colors (filled color symbols; Plez et al. 2003) of different temperatures: 4000, 3800, 3600, 3400, 3200, 3000 K. The black solid curve from lower left to upper right is the line joining all models with C/O ratio of 0.97. The π^1 Gruis color range is enclosed in the dashed box.

3.3. Analytical modeling

Now that the MARCS intensity distribution of π^1 Gruis is known, it can be used to model the spectro-interferometric measurements of the star.

3.3.1. The analytical thin-dusty-shell model

The general expression of the analytical thin-dusty-shell intensity distribution was derived by Cruzalèbes & Sacuto (2006). These authors present an analytical solution to the radiative transfer equation in spherical geometry for an optically thin dusty shell. The model, briefly explained below, was compared to the well-established radiative transfer code DUSTY used to fit the spectro-interferometric data of π^1 Gruis (see Sect. 3.4.1). Using this thin-dust-shell model is justified by the low mass-loss rate of the star (4.6×10^{-7} M$_\odot$ yr^{-1}; Jorissen & Knapp 1998) in view of the low-contrast, mid-infrared emission features. This led Gail (1990) to propose that the dust formation is insufficient for triggering a dust-driven outflow. The advantage of this model is the straightforward way a first set of physico-chemical parameters can be determined along with their errors. These output parameters are then inserted into the widely-used numerical radiative transfer code DUSTY in order to confirm and complete the analysis of this star (see Sect. 3.4).

The expression of the intensity given by the analytical thin-dusty-shell model is described in Sect. 2.2 in Cruzalèbes & Sacuto (2006), where the central star is represented by the corresponding synthetic MARCS S-spectrum (see Sect. 3.2). The global optical depth related to the infrared continuum excess is given by

$$\tau_\lambda^{\rm out}(\varepsilon) = \kappa_{\lambda_0}^{\rm in}\left(\frac{\lambda}{\lambda_0}\right)^{-\beta}\left(\frac{\varepsilon_{\rm in}}{\varepsilon_{\rm out}}\right)^{p} l^{\rm out}(\varepsilon), \tag{3}$$

where $\kappa_{\lambda_0}^{\rm in}$ is the extinction coefficient at the inner boundary at the reference wavelength λ_0. The extinction coefficient is parametrized as a decrease with wavelength as $\lambda^{-\beta}$. Values of β are usually taken between 0.2 and 2.4 depending on the chemistry, nature (amorphous or crystalline), shape, and size of grains (Dupac et al., 2003). The factor p corresponds to the radial number density falling off as r^{-p}. The parameters $\varepsilon_{\rm in}$ and $\varepsilon_{\rm out}$ are the angular radii of the shell inner and outer boundaries, respectively. Finally, $l^{\rm out}(\varepsilon)$ is the total geometrical depth of the shell.

The formalism described in Cruzalèbes & Sacuto (2006) applies in the context of the infrared continuum excess caused by the dust shell. However, as we can see in Fig. 1, the spectrum of π^1 Gruis exhibits a bump around 11 μm caused by the emission from oxygen-rich dust. The optical depth of this bump can be modeled with a Gaussian distribution (Groenewegen et al., 1994),

$$\tau_\lambda^{\rm bump} = A\ e^{-\left(\frac{\lambda-\lambda_{\rm c}}{\Delta\lambda}\right)^2}, \tag{4}$$

where A is the strength of the bump, $\lambda_{\rm c}$ the central wavelength of the dust feature, and $\Delta\lambda$ related to the width of the bump. Therefore, the expression for the intensity must depend not only on the optical depth related to the infrared continuum excess (Eq. 3) but also on the optical depth related to the mid-infrared bump (Eq. 4). In the case of spherical symmetry, the visibility function V_λ measured by an interferometer is linked to the angular distribution of the intensity of the source $I_\lambda(\varepsilon)$ through the normalized Hankel transform,

$$V_\lambda\left(\frac{b_{ij}}{\lambda}\right) = \left|\frac{\breve{I}_\lambda\left(\frac{b_{ij}}{\lambda}\right)}{\breve{I}_\lambda(0)}\right|, \tag{5}$$

where b_{ij} is the modulus of the projected baseline (on the plane of the sky) formed by the pair of apertures $(i;j)$, and

$$\breve{I}_\lambda(f) = \int_0^\infty 2\pi\varepsilon I_\lambda(\varepsilon)\, J_0(2\pi f\varepsilon)\, d\varepsilon \tag{6}$$

is the Hankel transform of I_λ at the spatial frequency $f = b_{ij}/\lambda$, where J_0 is the zeroth-order Bessel function of the first kind. Note that $\breve{I}_\lambda(0)$ corresponds to the flux density of the source F_λ.

The aim of this model is to give a first set of physico-chemical parameters by simultaneously fitting spectrometric and interferometric data. These parameters are then used as input parameters in the numerical code DUSTY to determine the final set of parameters characterizing the dusty circumstellar environment of π^1 Gruis.

The independent parameters of the models can be determined using the well-known iterative Levenberg-Marquardt algorithm minimizing the χ^2 function obtained by comparing modeled and measured visibilities, using the weight associated with the N visibility measurements. These weights are determined by the inverse square of the visibility errors. The minimization process uses the analytical expressions for the first derivatives of the visibility function with respect to each independent parameter as extensively described in Cruzalèbes & Sacuto (2006).

3.3.2. Spectro-interferometric results

In this section, the π^1 Gruis interferometric data are analyzed by means of the analytical model described in Sect. 3.3.1. The fit is done separately on two data sets, referred to as *DATA_SPECTRO_CAL* and *DATA_INT_CAL* in the following. The former set corresponds to the π^1 Gruis MIDI data calibrated with the 26.8 ± 1.3 mas diameter of β Gruis derived from the spectrometric method (see Appendix A.1). The latter set is calibrated with the 28.8 ± 0.6 mas diameter of β Gruis derived from the interferometric method (see Appendix A.2).

Some parameters of the analytical model were fixed at pre-determined values or only allowed to vary within a reasonable range:

- The effective temperature ($T_{\rm eff}$), which was found to be 3000 to 3100 K both from the work of Vanture & Wallerstein (2002) and from the position of the star in the (J-K,V-K)$_0$ color-color diagram. Therefore both 3000 and 3100 K synthetic MARCS models were utilized for the fit.
- A dust temperature at the inner boundary ($T_{\rm in}$) between 600 and 800 K, in accordance with the low mass-loss rate of this star for which dust condensation will halt at an intermediate stage of the condensation-ladder (see Sect. 3.4.2). This is called the "freeze-out" mechanism (Heras & Hony, 2005; Blommaert et al., 2006).
- The central wavelength of the dust feature ($\lambda_{\rm c}$), which is fixed to 11 μm from the position of the mid-infrared bump excess (see Fig. 1).
- Varying the density power-law coefficient (p) between 1 and 2.5.
- Varying the value of the spectral index (β) between 0.2 and 1.4, in agreement with values observed in circumstellar environments (Weintraub et al., 1989; Beckwith et al., 1990; Knapp et al., 1993).

The model provides in both cases good quality fits ($\chi^2/(N-p) = \chi^2_{\rm red}$<0.6, where N is the number of measurements and p is the number of adjustable parameters); however, the parameter values are relatively different for the two data sets, especially for the central star diameter. Because this parameter is the most constraining for the stellar spectrum, one can easily distinguish which of the parameter sets provides the most reliable fit to the spectrum of the star by superimposing the analytical flux model generated with the 2 parameter sets onto the spectro-photometric data of the star. Figure 6 compares the π^1 Gruis fluxes predicted by the analytical model using the parameters for the data sets *DATA_SPECTRO_CAL* or *DATA_INT_CAL*, with the MIDI flux, the ISO/SWS spectrum, and the photometric data. It is very clear from this figure that the parameter set providing the best fit to the spectrum is the *DATA_SPECTRO_CAL* one (see Table 4).

Table 4. Parameters of π^1 Gruis deduced from the fit of the analytical visibility model to the data sets *DATA_SPECTRO_CAL*.

Parameter	Value
Effective temperature (K) : $T_{\rm eff}$	3000
Luminosity ($L_\odot$) : $L_\star$	9300±2700
Central star diameter (mas) : 2 $\varepsilon_\star$	21.6±0.3
Shell inner radius (mas) : $\varepsilon_{\rm in}$	159±10
Inner boundary temperature (K) : $T_{\rm in}$	776±25
Dust bump wavelength (μm) : $\lambda_{\rm c}$	11*
Bump amplitude ($\times 10^{-4}$) : A	8.3±0.6
Bump width (μm) : $\Delta\lambda$	2.8±0.3
Bump optical depth ($\times 10^{-3}$) : $\tau_{11\mu{\rm m}}$	1.5±0.2
Density power law coefficient : p	1.7
Spectral index : β	1
$\chi^2_{\rm red}$	0.55

$*$: fixed at pre-determined value.

The stellar diameter obtained from the fit of the analytical model is ϕ=21.6 mas. This corresponds to $R_\star$=357 $R_\odot$ for the adopted Hipparcos distance of D=153 pc. In a study of the angular size of a sample of S and C stars, Van Belle (1997) found that, for non-Mira stars, S-type stars are on average 110 $R_\odot$ larger than M-type stars. Since the relationship between radius and $V-K$ color derived by Van Belle (1999) applies to M stars, the corresponding radius of π^1 Gruis is set to 359 $R_\odot$, a value very close to the one obtained from the fit of the analytical model. In Table 4, the luminosity of the central star has been added. This one is deduced from the effective temperature of the central star ($T_{\rm eff}$=3000 K), its angular diameter ($\phi_\star$=21.6±0.3 mas), and its distance (D=153±20 pc),

$$L_\star = 4\pi \left(\frac{\phi_\star}{2} D\right)^2 \sigma T_{\rm eff}^4 \approx (9300 \pm 2700) L_\odot, \quad (7)$$

where σ is the Stefan-Boltzmann constant. The corresponding apparent bolometric magnitude of π^1 Gruis is 0.8±0.6, in agreement with the value of 1.07 found by Van Eck et al. (2000b).

Another significant parameter value is the density power-law coefficient. With an $r^{-1.7}$ density distribution, this suggests a decrease in mass-loss rate with time, in line with the finding of Chiu et al. (2006) that the mass-loss rate of π^1 Gruis has probably decreased over the past 90 years. This set of parameters will thus be used as input for the DUSTY model described in Sect. 3.4.1.

3.4. Numerical modeling

3.4.1. The DUSTY code

The DUSTY code (Ivezić et al., 1999) was used to generate synthetic spectrally-dispersed (8-13 μm) flux and visibilities to confirm and complete the parameter set found with the analytical model (see Table 4). DUSTY is a public-domain simulation code that solves the problem of radiation transport in a circumstellar dusty environment by integrating

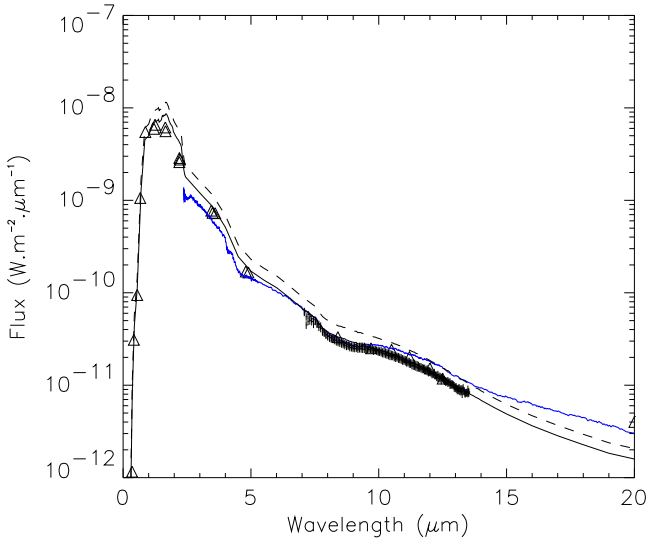

Fig. 6. Comparison of the π^1 Gruis fluxes predicted by the analytical model using the parameters for the data sets *DATA_SPECTRO_CAL* (solid line) or *DATA_INT_CAL* (dashed line), with the MIDI flux (error bars), the ISO/SWS spectrum (blue line), and the photometric data (open triangles).

the radiative transfer equation in plane-parallel or spherical geometries (Ivezić & Elitzur, 1997; Ivezić et al., 1999).

The DUSTY model integrates the MARCS synthetic stellar spectrum of the central star (see Sect. 3.2) and considers as input parameters a part of those deduced from the fit of the analytical model: $T_{\rm eff}$, $L_\star$, $T_{\rm in}$, $\tau_{11\mu m}$, and p (see Table 4). DUSTY also requires the grain size distribution as input so we chose a standard MRN grain size distribution as described by Mathis et al. (1977): $n(a) \propto a^{-3.5}$ with minimum and maximum grain sizes of 0.005 μm and 0.25 μm, respectively.

Therefore, the analytical model allows one to reduce the number of DUSTY input parameters from 8 to 2 (namely the chemical composition of the dust and the thickness of the shell). Indeed, the chemical composition of the dust is related to the value of the spectral index β. However, this value encapsulates many characteristics related not only to the chemistry of the grains but also to their nature (amorphous or crystalline), their shapes, and their sizes.

The thickness of the shell was found to be the least accurate output parameter, with a lower limit of 60 stellar radii, corresponding to the beam size of an AT. In fact, varying this value from 60 to 1000 times the stellar radius does not have a significant impact on the model. This is related to the low mass-loss rate of π^1 Gruis (4.6×10^{-7} $M_\odot\,yr^{-1}$) leading to a very low dust density in the outer layers. Since the N band is not well-suited to determining the outer radius of the dust shell, this one could extend to the inner radius of the flared disk located at 125 stellar radii (Chiu et al., 2006).

3.4.2. Dust chemical composition

The last free parameter to determine for the DUSTY modeling is the chemical composition of the dust shell. However, this parameter can be constrained from the shape of the mid-infrared spectrum.

The classification by Little-Marenin & Little (1988, 1990) (hereafter referred to as the LML classification) gives a sequence from the classic, narrow-emission feature at 10 μm (classified as silicate) to features with progressively stronger contributions at 11 μm (silicate+ and silicate++, depending on its strength) to broad, low-contrast emission peaking longward of 11 μm (Broad). In this classification, Little-Marenin & Little (1988) investigate the LRS (IRAS Low-Resolution Spectrometer) spectra of a large number of MS and S stars and suggest that the unusual dust chemistry (caused by a C/O ratio near unity) might produce unusual dust excess. Little-Marenin & Little (1988) create a separate class of silicate emission, the S class, which they associate with S stars and describe as having a peak emission around 10.8 μm, which is the case for π^1 Gruis (see Fig. 1). However, later analysis by Chen & Kwok (1993) and Sloan & Price (1995) concluded that the LRS spectra of S stars are not significantly different from those of M giants. Sloan & Price (1998) noticed that MS and S stars, having a C/O ratio near unity, produce circumstellar shells dominated by alumina grains. They suggest that, when the C/O ratio approaches unity, the formation of CO leaves little oxygen available for grain formation. As gaseous material moves away from the central star and cools, alumina grains will form before silicate grains because of the higher condensation temperature of alumina. Sloan & Price (1998) also suggest that stars with C/O ratios near unity may exhaust the supply of available oxygen with the formation of CO gas and alumina grains, preventing silicates from forming.

Figure 1 shows the broad dust emission feature from 9 to 13 μm peaking at 10.5 μm, which originates from the optically and geometrically thin shell of π^1 Gruis. This spectral shape is well-known and corresponds to one phase of the *silicate dust sequence* scenario (hereafter referred to as the SDS scenario) introduced by Stencel et al. (1990). In this scenario, grains form first from condensing alumina material. Then, as the grains evolve, silicate material begins to dominate the emission. Fresh silicate material would be crystalline and exhibit rather narrow emission components at 10 and 11 μm, while grains in more extended shells would be amorphous and exhibit the classic silicate feature. The S star π^1 Gruis belongs to the bottom end of the SDS, classified as SE2 by Sloan & Price (1998). This lower silicate dust sequence is populated by spectra with broad, low-contrast emission features, originating from optically thin shells of alumina dust.

In this context, we first tried to reproduce the mid-infrared spectral shape emission with a pure alumina shell using porous amorphous Al_2O_3 of Begemann et al. (1997)[2] retrieved from the Database of Optical Constants of the Laboratory Astrophysics Group of the AIU Jena[3]. This

[2] Note that the data of Begemann et al. (1997) only cover emission between 7.8 and 500 μm. DUSTY assumes a constant refractive index in the unspecified shorter wavelength range, with a value equal to the corresponding first point of the tabulation.

[3] `http://www.astro.uni-jena.de/Laboratory/Database/`

Table 5. Parameters for π^1 Gruis deduced from the fit of the DUSTY model to the interferometric and spectrophotometric data.

Parameter	Value
Effective temperature (K)	3000^+
Luminosity ($L_\odot$)	8700^+
Central star diameter (mas)	21.0
Shell inner radius (mas)	149.5
Inner boundary temperature (K)	700^+
Grain chemical composition	70% WS + 30% Al. [1]
Density power law coefficient	1.7^+
Grain size distribution	MRN*
Geometrical thickness ($\varepsilon_\star$)	60^2
11 μm optical depth ($\times 10^{-3}$)	8.3^+

$*$: fixed at pre-determined value.
$+$: derived from the analytical model (see Table 4).
[1]WS stands for warm silicates and Al. for alumina.
[2]This value is not well defined (see text).

composition failed to fit the spectrometric data. Spectra of SE2 class stars do not exhibit any emission peak at 10 μm. However, the ISO/SWS and MIDI spectra of π^1 Gruis show that the emission feature begins to peak at 10 μm, ending beyond 12 μm (see Fig. 1). Therefore, in spite of the SDS classification of π^1 Gruis as SE2, it seems that this star is close to the *structured* silicate emission class (SE3-SE6). This class is intermediate between the *silicate* and the *broad* class stars implying that the model contains a mixture of silicate and alumina grains, as discussed by Lorenz-Martins & Pompeia (2000). Consequently, we decided to work with mixtures of aluminum oxide and warm silicate (Ossenkopf et al., 1992), ranging from 100% alumina grains to 100% silicate grains in 10% increments. We find a good fit (see Fig. 7) with a ratio of 30% alumina and 70% silicate grains (see Table 5).

The 11 μm global optical depth found with the analytical method ($\tau_{11\mu m}$=(1.5±0.2)×10^{-3}; Table 4) appears to be somewhat too small for DUSTY, which requires about 5 times more optical depth to yield a good fit of the IR spectrum. This may be due to the analytical model assuming that the 11 μm feature may be approximated by a Gaussian function, whereas Fig. 1 shows that this excess is clearly asymmetric.

The temperature at the inner boundary of the shell (700 K; Table 5) is below the aluminum oxide ($T_{cond}^{Al_2O_3}$≈1500-1800 K) and silicate (T_{cond}^{Si}≈1000-1500 K) condensation temperatures. Such low temperatures in the shells of evolved stars were first suggested by Rowan-Robinson & Harris (1982) and later by Onaka et al. (1989) and Simpson (1991), based on studies of the IRAS/LRS data. Onaka et al. (1989) argue that these low temperatures cannot be understood in the framework of homogeneous nucleation theories and propose, as a possible explanation, that mantle growth on pre-existing aluminum oxide particles is the major process of silicate formation. Extending the temperature at the inner boundary of the shell to alumina condensation temperature (∼1500 K) can also explain both the spectrum and visibility of the star. However, assuming a mass-loss rate value of $4.6\times10^{-7} M_\odot\,yr^{-1}$ for π^1 Gruis (Jorissen & Knapp, 1998) and a dust-particle specific density of 3 g cm^{-3}, the value of the gas-to-dust ratio of the model is 60. We obtain a value of 165 for the inner boundary temperature of 700 K, which agrees with the gas-to-dust ratio of 158±13 obtained by Knapp (1985) for oxygen stars.

Figure 7 shows the best interferometric and spectrophotometric fit of the DUSTY model corresponding to the parameter set of Table 5. The model appears to match the observed spectra well and the MIDI visibilities fairly well. However, while the spectral fit of the DUSTY model is good overall but especially so in the mid-infrared band (8-13 μm), the model visibilities are over-evaluated for the two ∼15 and 30 m projected baselines in the 8-9 μm spectral band (see Fig. 7). This reveals that the model is not extended enough for these baselines at these wavelengths. This can be explained by the very low optical depth in that spectral range ($\bar{\tau}$(8-9 μm)=2.5×10^{-3}) leading to a domination of the central star flux over the flux of the dust shell. In the 8-9 μm spectral range, the model therefore has values very close to the central star's uniform-disk intensity distribution, leading to an increase in the visibility. Moreover, one can see that the 8-9 μm visibilities decrease with the increase in the baseline lengths, which is understandable in the context of an equivalent uniform-disk visibility function.
A way to increase the spatial extension of the model between 8 and 9 μm is to add a molecular shell between the photosphere of the star and the inner boundary of the dust shell. In the next section, we investigate the possibility of adding such a molecular shell in the model.

3.5. Addition of a warm H_2O+SiO molecular shell

Recent work reveals that diameters of the Mira and non-Mira stars appear systematically larger than expected in the near-infrared (Mennesson et al., 2002; Ohnaka, 2004b; Perrin et al., 2004; Weiner, 2004) and in the mid-infrared (Weiner et al., 2000, 2003a,b; Weiner, 2004; Ohnaka, 2004b; Ohnaka et al., 2005). Such an increase cannot be attributed only to dust shell features, but also to the possible existence of extended gaseous shells close to the stellar photospheres. The analyses of the spectra obtained with ISO/SWS have revealed that the spectra of Mira variables are well-reproduced by water vapor shells extending to 2-4 stellar radii with gas temperatures of 1000-2000 K and column densities of 10^{20}-10^{22} cm^{-2} (Tsuji et al., 1997; Yamamura et al., 1999; Matsuura et al., 2002). Since π^1 Gruis is a non-Mira star, we should expect different parameter values than those for Mira variables.
The single dust shell modeling with DUSTY (see Fig. 7) suggests that we need to have a contribution from a molecular shell only in the 8-9 μm spectral band. Such a molecular shell, also called "MOLsphere" (Tsuji et al., 2000), is favored by the low surface gravity (log g=0; see Table 3) and high luminosity (∼9000 $L_\odot$) of the star, allowing the levitation of the upper layers. The temperatures in this levitated matter can be low enough for molecules to form (Verhoelst et al., 2006).

Because this molecular shell has a larger extent than the central star, the former is resolved with smaller baselines so as to decrease the visibility amplitudes in that spectral range. At the same time, the molecular shell must make a negligible contribution to the total flux in the 9 to 13 μm spectral range relative to the dust shell, to recover the good fit that we found with

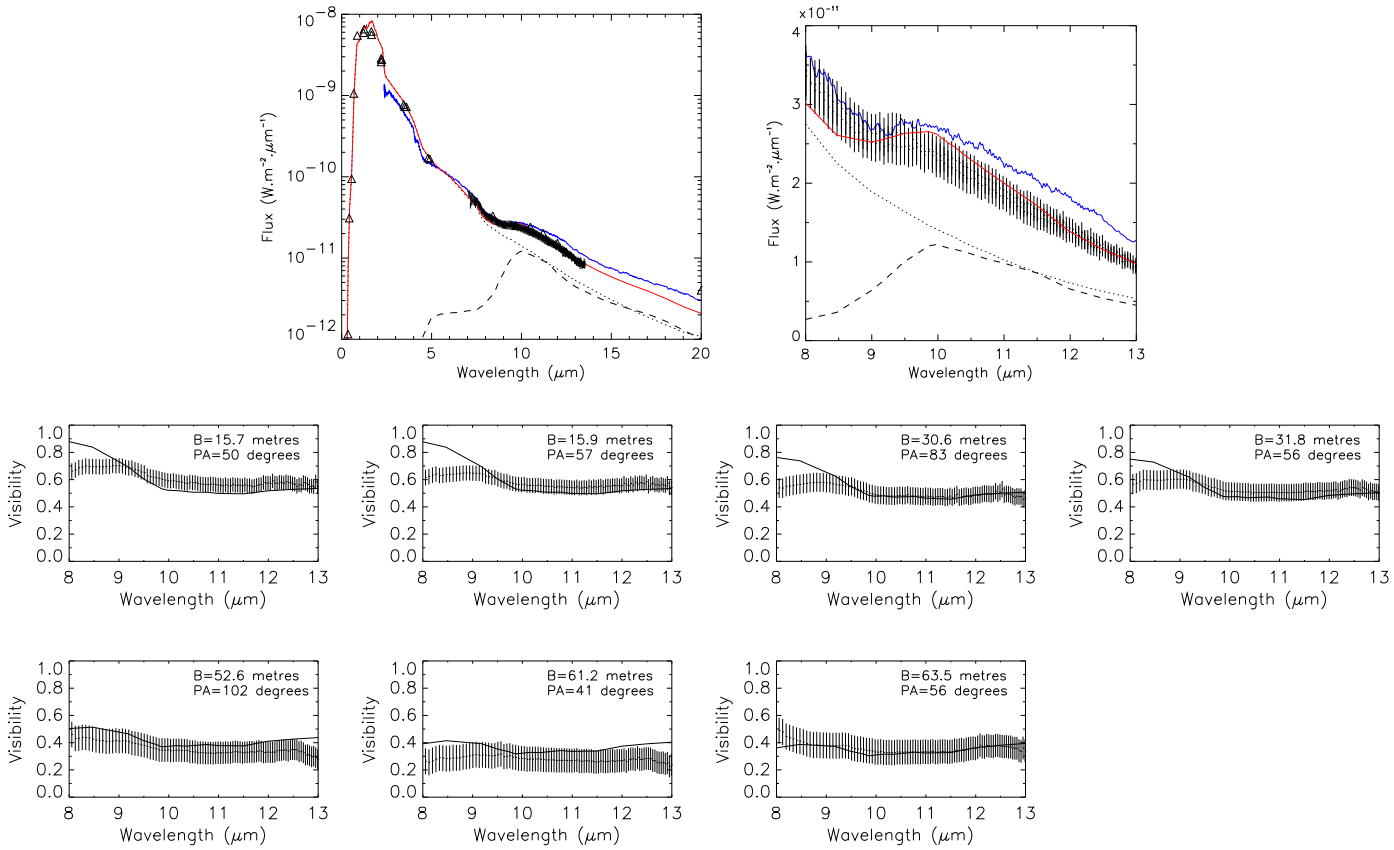

Fig. 7. Top-left: best fit of the dust shell model spectrum (red line) on the MIDI flux (error bars), the ISO/SWS spectrometric data (blue line), and the photometric data (open triangles) of π^1 Gruis. The central star contribution (dotted line) and the dust shell contribution (dashed line) are added. Top-right: close-up view of the best fit of the dust feature. Bottom: the corresponding model visibility (solid line) superimposed on the MIDI visibilities (error bars) for the seven projected baselines.

the single dust shell model at these wavelengths (see Fig. 7).

Water vapor (H_2O) and silicon monoxide (SiO) are the main molecules contributing to absorption and causing the apparent mid-infrared diameter to be larger than the continuum diameter (Ohnaka et al., 2005; Verhoelst et al., 2006; Perrin et al., 2007). The H_2O lines are present across the entire N band range, while most SiO lines are located between 8 and 10 μm.

The model of molecular shell that we chose is the same as the one used by Ohnaka et al. (2005) and consists of H_2O and SiO gas with constant temperature and density, extending from the central star radius up to the external boundary $\varepsilon_{\rm mol}$. The input parameters of the model are the temperature of the molecular shell ($T_{\rm mol}$), the column densities of H_2O and SiO ($N_{\rm col}^{H_2O}$ and $N_{\rm col}^{SiO}$, respectively) in the radial direction, and the geometrical extension of the shell ($\varepsilon_{\rm mol}$).
In this model, we first calculate the line opacity due to H_2O and SiO with a wavenumber interval of 0.04 cm^{-1} over a wavelength range between 8 and 13 μm. We adopt a Gaussian line profile with an FWHM of 5 km s^{-1}, which represents the addition of a gas thermal velocity of a few km s^{-1} (V_T=1.5($T_{\rm mol}$/300 K)$^{0.5}$ km s^{-1}) and the micro-turbulent velocity in the atmosphere of π^1 Gruis (3 km s^{-1}; see Table 3) and assumes that the molecular gas is in local thermodynamical equilibrium. The list of H_2O lines was taken from the HITEMP database (Rothman, 1997) while that of the fundamental bands of SiO was generated from the Dunham coefficients given by Lovas et al. (1981) and the dipole moment matrix elements derived by Tipping & Chackerian (1981).

The resulting intensity distribution of the object is composed of the central star with a MARCS model atmosphere, the molecular shell, and the dust shell. The analytical expression of the model is given by the expressions below:

$$I_\lambda^\star(\varepsilon) = I_\lambda^{\rm marcs} e^{-\tau_{\rm mol}} e^{-\tau_{\rm dust}} \ \Pi\left(\frac{\varepsilon}{2\varepsilon_\star}\right) \quad (8)$$

$$I_\lambda^{\rm mol}(\varepsilon) = B_\lambda(T_{\rm mol})\ e^{-\tau_{\rm dust}}\left[1-e^{-\tau_{\rm mol}}\right]\ \Pi\left(\frac{\varepsilon}{2\varepsilon_{\rm mol}}\right) \quad (9)$$

$$I_\lambda^{\rm dust}(\varepsilon) = B_\lambda(T_{\rm dust})\left[1-e^{-\tau_{\rm dust}}\right]\ \Pi\left(\frac{\varepsilon}{2\varepsilon_{\rm out}}\right) \quad (10)$$

where $\tau_{\rm mol}$ and $\tau_{\rm dust}$ are the optical depths of the molecular and dust shells, respectively, and Π is the uniform disk distribution ($\Pi(x) = 1$ if $-1/2 < x < 1/2$, zero otherwise). The corresponding flux and visibility, obtained by the Hankel transform of the intensity profile, are then spectrally convolved to match the low spectral resolution (30) of the MIDI prism. Using the above model and without

Table 6. Best combination of input values for the determination of the molecular shell.

Component	T_{mol} (K)	ε_{mol} ($\varepsilon_\star$)	N_{col} (cm^{-2})
H_2O	1000	4.4	5×10^{18}
SiO	-	-	2×10^{18}

changing the parameter values found for the thin dust shell (see Table 5), we search for the best combination of input parameters (T_{mol}, ε_{mol}, $N_{col}^{H_2O}$, and N_{col}^{SiO}) to improve the spectro-interferometric fitting in the 8-9 μm spectral range. The best-fitting values are presented in Table 6.

These values correspond to an extended, optically thin (τ_{mol}<0.1) molecular shell. Such a diluted molecular shell can be connected to the nature of π^1 Gruis. First, because the C/O ratio is close to unity for S stars (C/O=0.97 for π^1 Gruis; see Fig. 5), the last oxygen-bearing molecules disappear (Ferrarotti & Gail, 2002). Second, due to its classification as a non-Mira semi-regular variable, for which the variability amplitudes are much smaller than for Mira variables, a less dense molecular shell is indeed expected. From these arguments, it seems reasonable that this star exhibits weak spectral features from the molecular shell.

Figure 8 shows our best spectrometric and interferometric fit to the optically thin H_2O+SiO molecular shell and optically thin silicate+alumina dust shell model using the parameter sets of Tables 5 and 6.

This figure reveals that the spectrometric, as well as the visibility measurements are now well-reproduced over all the 8-13 μm spectral band for all projected baselines. In particular, the model visibilities have decreased in the 8-9 μm spectral band compared to the single dust shell model (see Fig. 7). This is due to the correlated flux contribution of the molecular shell leading to a more extended object at these wavelengths. With a size of 4.4 stellar radii, the molecular shell is almost completely resolved with baselines larger than 30 meters. For this reason, its contribution to the correlated flux is greater for the 15- and 30-meter projected baselines than for the 60-meter one. The optical depth of the molecular shell outside the 8 to 9 μm range is ten times less than in this band. Therefore, the correlated flux contribution of the molecular shell is almost negligible at these wavelengths, preserving the good fit from the single dust shell model.

From this last model, we can now infer the spatial circumstellar structure of π^1 Gruis. It consists of an optically thin warm H_2O+SiO molecular shell extending from the stellar photosphere out to 4.4 stellar radii, then an optically thin alumina-silicate dust shell beginning at about 14 stellar radii, and finally a slowly expanding flared disk with a central cavity of radius about 125 stellar radii, determined by Chiu et al. (2006) in the millimetric spectral range.

4. Asymmetries of the circumstellar material and binarity

The bipolar outflow perpendicular to the flared disk was discovered by Sahai (1992) and subsequently studied by Knapp et al. (1999a) and Chiu et al. (2006). A similar structure combining disk and jet was observed by Knapp et al. (1997) in another very evolved AGB star, V Hya, whose binary nature was subsequently discovered by Knapp et al. (1999b). As argued by Huggins (2007), the binarity seems to be a necessary condition creating a disk/jet structure in evolved mass-losing stars. Although π^1 Gruis has a G0V companion located 2.71″ away, this companion falls within the expanding disk (Chiu et al., 2006), a strange situation that has not been encountered in, for example, binary post-AGB stars, where the companion falls well within the cavity interior to the disk (Waelkens et al., 1996; Dominik et al., 2003). Therefore, Chiu et al. (2006) wonder whether there 'might be a much closer companion that has so far escaped detection and currently is the source of the high-velocity outflow'.
Makarov & Kaplan (2005) and Frankowski et al. (2007) find possible evidence for such a close companion from the discrepancy between the Hipparcos and Tycho-2 proper motions. The Hipparcos proper motion relies on measurements only spanning 3 years, whereas the Tycho-2 one uses positional data spanning more than a century. Any discrepancy between these short-term and long-term proper motions is thus indicative of an unrecognized orbital motion in addition to the true proper motion. The discrepancy is very significant in the case of π^1 Gruis. According to the analysis of Frankowski et al. (2007), these so-called '$\Delta\mu$ binaries' correspond to systems with orbital periods in the range 1500-10^4 days, much shorter than the 6000 years period inferred by Knapp et al. (1999a) for the G0V companion 2.7″ away.

We now estimate the likely range for the orbital separation of the putative close companion and compare it to the size of the various shells and to the stellar radius. The period range for $\Delta\mu$ binaries with known orbital elements are from 1500 to 10000 days, according to Fig. 4 of Frankowski et al. (2007). Adopting a total mass of 2 $M_\odot$ for the system, the corresponding range in relative semi-major axes are 3.2 to 11.4 AU, or 20.8 to 74.4 mas (for the parallax of 6.5 mas). Adopting 3 $M_\odot$ instead yields 3.7 to 13.1 AU or 24 to 85 mas. These values must be compared to the

- stellar radius = ε_{star} = 10.5 mas
- H_2O+SiO molecular radius = 4.4 ε_{star} = 46.2 mas
- inner dust shell radius = 14.2 ε_{star} = 149.5 mas.

It is seen that only the longest periods and highest total masses are compatible with the shell sizes. One can wonder what in this case would be the impact of a companion orbiting at about 80 mas from the central star on the molecular and dust shell. As the extended dust shell is over-resolved, only the molecular shell could provide some hints of the presence of a perturbation. However, the mass-loss rate is so low that a high dynamic range is required to detect the asymmetries from the faint contribution from the molecular and dusty material. Such a dynamic range cannot correctly be achieved with the current MIDI capabilities. Nevertheless, the constraints provided by the differential phases that do not exhibit any obvious departure from spherical symmetry (see Fig. 3) have to be considered, since it is more sensitive to any departure from centro-symmetry.
The $\Delta\mu$ method offers no way to infer the position angle of the companion. However, if it is powering the jet, its orbital plane is likely to be coincident with that of the flared disk. The MIDI interferometric *uv* coverage (PA=41 to 102°) is oriented in the direction of the flared disk

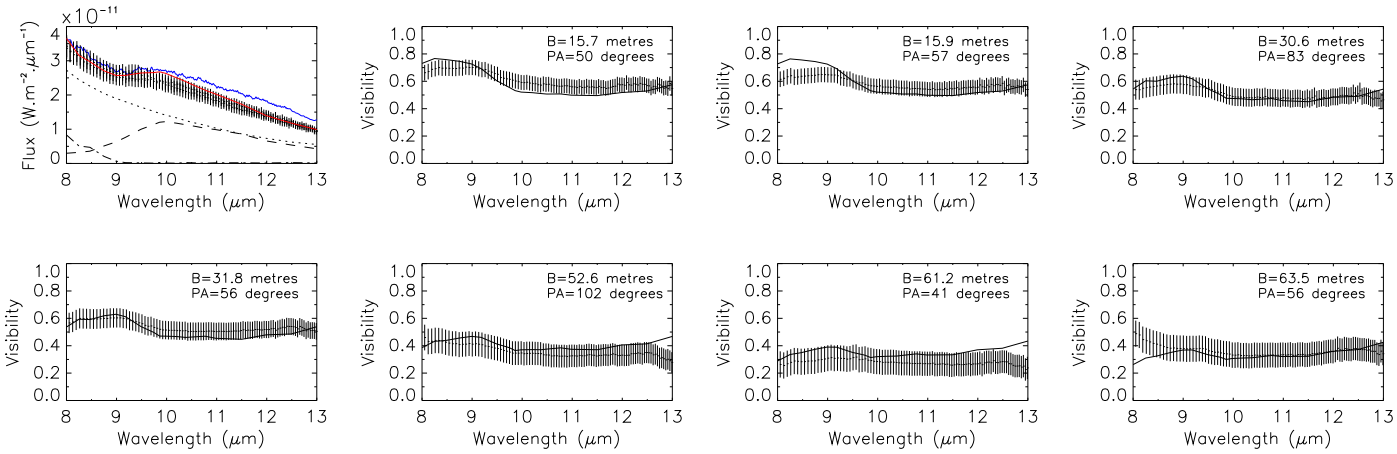

Fig. 8. Top-left: best fit of the proposed H_2O+SiO molecular shell and silicate+alumina dust shell model spectrum (red line) on the MIDI flux (error bars) and the ISO/SWS spectrometric data (blue line) of π^1 Gruis. The central star contribution (dotted line), the molecular shell contribution (dot dashed line), and the dust shell contribution (dashed line) are added. The other figures show the corresponding model visibility (solid line) superimposed on the MIDI visibilities (error bars) for the seven projected baselines.

(and thus along the orbital plane), as deduced from Fig. 4 in Chiu et al. (2006). It is then difficult to envisage the presence of a close companion without any detection of asymmetries. This could be the case if the dust shell were not heated by the companion, which must therefore be on the lower main sequence (cool and faint).

Beyond there being no detection of asymmetries as shown by the zero-differential phase (see Fig. 3), there is a more fundamental information inferred from the interferometric observations in Fig. 4. There is no obvious indication that the star alone could drive the jet and shape its surrounding. Notwithstanding this fundamental constrain, we are left with two possibilities, each of them invoking the influence of a companion:

(i) There is indeed a close companion (cool and faint) to power the jet, but then why are there no departures from spherical geometry close to the star, related to the presence of an accretion disk?

(ii) The close $\Delta\mu$ companion is spurious, but then the jet must be powered by the far-away companion, and why is this outer companion orbiting the disk without creating a gap in it, as would be evident in the millimetric observations?

Regarding item (i), one explanation could come from the close, optically thin environment of π^1 Gruis leading to similar SEDs for accretion disks and spherical dust shells, as discussed by Knapp et al. (1993) and van der Veen et al. (1994). If we add to this argument the fact that the *uv* coverage is preferentially oriented in the direction of the disk having an opening angle larger than the interferometric angular coverage ($\sim$60°), it is then easy to confuse this structure with a spherical shell.

Regarding item (ii), it must be mentioned that the $\Delta\mu$ method might face problems when dealing with highly evolved stars and might then yield spurious results. To substantiate this, notice that Table 8 of Frankowski et al. (2007) lists several other candidate $\Delta\mu$ binaries among long-period variables and suggests that these detections are similarly spurious, although the reason thereof remains unidentified.

Still, even in the absence of a close companion, the Huggins (2007) analysis of the jet/torus properties in several AGB stars (among which π^1 Gruis) and proto-planetary nebulae requires them to be binaries. The 2.7″ companion to π^1 Gruis must then be the one responsible for driving the jet/torus structure. In that case however, the conclusion of the CO data analysis by Chiu et al. (2006), which locates the companion *within* the flared disk, is quite surprising (when compared to situations prevailing in post-AGB systems for instance). Such a situation cannot be stable in the long term since the companion should carve a gap in the disk. If correct, it indicates that the disk is quite young, as confirmed from its kinematics. Taking into account a mean value of 11 $\mathrm{km\,s^{-1}}$ for the wind expansion velocity found by Chiu et al. (2006) and a distance of 153 parsec (Perryman et al., 1997), we can estimate the typical transit time of the dust shell to be about 10 years, while the flared disk age is about 350 years (Huggins, 2007) with a strong decrease in the mass-loss rate about 90 years ago (Chiu et al., 2006).

5. Summary and conclusions

The goal of this work was to perform a multi-wavelength and multi-spatial resolution study of the close environment of π^1 Gruis with the N band spectral range of MIDI. Our new high spatial-resolution observations of the environment of π^1 Gruis, consisting of MIDI/VLTI spectra and visibilities, combined with the existing millimeter data, led to a more comprehensive picture of its circumstellar environment on different spatial and spectral scales.

A preliminary study of MIDI data shows that the mas-scale observations do not reveal any strong departure from the sphericity of the circumstellar environment, whereas arcsec-scale millimetric observations by Knapp et al. (1999a) and Chiu et al. (2006) show strong evidence of a slow and dense outflow (v$\sim$15 km s^{-1}) and of a fast bipolar ejection (v$\geq$90 km s^{-1}). Even though the constraints provided by these interferometric observations are limited in terms of *uv* coverage and dynamics, this suggests that the companion located at 2.7″ (400 AU at 153 pc, i.e. far outside the MIDI interferometric Field-Of-View of about 175 AU) may have some influence on the shape of the large-scale CO environment and may possibly launch the fast outflow that has been detected (cf. the models of Mastrodemos & Morris 1999 and the discussion in Chiu et al. 2006).

The more detailed study starts with determining a synthetic atmosphere model for π^1 Gruis to obtain approximate physical characteristics of the central star. The dusty circumstellar environment was initially analyzed with the optically thin analytical radiative transfer model developed by Cruzalèbes & Sacuto (2006). This model allowed us to determine some parameter values related to the central star and its dust shell, which we used to generate a more refined model with the numerical radiative transfer code DUSTY. This code helped us to determine the chemical composition of the close circumstellar environment, which was one of the main aims of this study. We show, from the literature, that this star belongs to one phase of the SDS scenario (Sloan & Price, 1998), in which grains first form from condensing alumina material. We confirmed this tendency using spectro-interferometric fitting and derived a ratio of alumina to silicate dust of 0.4, revealing that π^1 Gruis is situated in an intermediate class named the *structured* silicate emission class.
We then included an optically thin H_2O+SiO molecular shell extending from the photosphere of the star up to 4.4 stellar radii with a typical temperature of 1000 K to account for the fact that the single dust shell model is not extended enough in the 8-9 μm spectral range. The formation mechanism of molecular shells in non-Mira semi-regular variables like π^1 Gruis, in which the variability amplitudes are much less than in Mira stars, can lead to less dense MOLspheres. Moreover, as S stars have a C/O ratio close to unity, neither oxygen-bearing nor carbon-bearing molecules are abundant in the atmosphere, with most of carbon and oxygen atoms locked up in CO molecules.

Complex structures revealed by millimetric observations suggest that π^1 Gruis may be at the end of its evolution on the AGB (Knapp et al., 1999a). This evolutionary stage is confirmed by the position of the star on the HR diagram of S stars (see Fig.7 of Van Eck et al. 1998). The large and diluted optically thin close environment around evolved stars could thus be part of the natural transition from the AGB to post-AGB and planetary nebulae stages. If this is true, what are the mechanisms responsible for such physical processes? Answers could come from long-term spectro-interferometric observations of the star and better Fourier *uv* coverage, which could be provided by the second generation VLTI instruments. This should be carried out in close synergy with ALMA array observations, which should provide images in the millimeter domain at similar angular resolution.

Acknowledgements. We would like to thank Brandon Tingley for the English revision of the text and S. Flament for his help on the data handling. Mr. Sacuto benefits from a PHD grant from the Conseil Régional Provence - Alpes - Côte d'Azur (France) managed by ADER-PACA.

References

Beckwith, S.V.W., Sargent, A.I., Chini, R.S., & Guesten, R., 1990, AJ 99, 924
Bedding, T.R., Robertson, J.G., & Marson, R.G., 1994, A&A 290, 340
Begemann, B. Dorschner, J., Henning, Th., et al., 1997, ApJ 476, 199
Blommaert, J.A.D.L., Groeneweggen, M.A.T., Okumura, K., et al., 2006, A&A 460, 555
Chen, P.S., & Kwok, S., 1993, ApJ 416, 769
Chen, B., Vergely, J.L., Valette, B., & Carraro, G., 1998, A&A 336, 137
Chiu, P-J., Hoang, C-T, Trung, D-V, et al., 2006, ApJ 645, 605
Chesneau, O., Meilland, A., Rivinius, T., et al., 2005, A&A 435, 275
Cruzalèbes, P., & Sacuto, S., 2006, A&A 452, 885
Davis, J., Tango, W.J., & Booth, A.J., 2000, MNRAS 318, 387
Dominik, C., Dullemond, C.P., Cami, J., & Van Winckel, H., 2003, A&A 397, 595
Dupac, X., Bernard, J.-P., Boudet, N., et al., 2003, A&A 404, 11
Egan, M.P., & Sloan, G.C., 2001, ApJ 558, 165
Engelke, C. W., 1992, AJ 104, 1248
Feast, M.W., 1953, MNRAS 113, 510
Feinstein, A., 1966, IBSH 8, 30
Ferrarotti, A.S., & Gail, H.-P., 2002, A&A 382, 256
Fitzpatrick, E.L., 1999, PASP 111, 63
Frankowski, A., Jancart, S., & Jorissen, A., 2007, A&A 464, 377
Gail, H.-P., 1990, Rev. Mod. Astron. 3, 156
Groenewegen, M.A.T., de Jong, T., & Gaballe, T.R., 1994, A&A 287, 163
Gustafsson, B., Bell, R.A., Eriksson, K., & Nordlund, A., 1975, A&A 42, 407
Heras, A.M., Shipman, R.F., Price, S.D., et al., 2002, A&A 394, 539
Heras, A.M., & Hony, S., 2005, A&A 439, 171
Huggins, P. J., 2007, ApJ 663, 342
Ivezić, Z., & Elitzur, M., 1997, MNRAS 287, 799
Ivezić, Z., Nenkova, M., & Elitzur, M., 1999, User Manual for DUSTY
Jaffe, W.J., 2004, SPIE 5491, 715
Johnson, H.L., Iriarte, B., Mitchell, R.I., & Wisniewskj, W.Z., 1966, CoLPL 4, 99
Jorissen A., & Knapp G.R., 1998, A&AS 129, 363
Judge, P.G., 1986, MNRAS 223, 239
Knapp, G.R., 1985, ApJ 293, 273
Knapp, G.R., Sandell, G., & Robson, E.I., 1993, ApJSS 88, 173
Knapp, G.R., Jorissen, A, & Young, K., 1997, A&A 326, 318
Knapp, G.R., Young, K., & Crosas, M., 1999a, A&A 346, 175
Knapp, G.R., Dobrovolsky, S.I., Ivezić, Z., et al., 1999b, A&A 351, 97
Leinert, C., Graser, U., Przygodda, F., et al., 2003, Ap&SS 286, 73
Little-Marenin, I.R., & Little, S.J., 1988, ApJ 333, 305
Little-Marenin, I.R., & Little, S.J., 1990, AJ 99, 1173
Lorenz-Martins, S., & Pompeia, L., 2000, MNRAS 315, 856
Lovas, F.J., Maki, A.G., & Olson, W.B., 1981, J. Mol. Spectros., 87, 449
Mastrodemos, N., & Morris, M., 1999, ApJ 523, 357
Mathis, J.S., Rumpl, W., & Nordsieck, K.H., 1977, ApJ 217, 425
Matsuura, M., Yamamura, I., Cami, J., et al., 2002, A&A 383, 972
Makarov, V.V., & Kaplan, G.H., 2005, AJ 129, 2420
Mendoza, E.E., 1969, BOTT 5, 57
Mennesson, B., Perrin, G., Chagnon, G., et al., 2002, ApJ 579, 446
Merrill, P.W., 1922, ApJ 56, 457
Mitchell, R.M., & Robinson, G., 1978, ApJ 220, 841
Ohnaka, K., 2004b, A&A 424, 1011
Ohnaka, K., Bergeat, J., Driebe, T., et al., 2005, A&A 429, 1057
Onaka, T., de Jong, T., & Willems, F.J., 1989, A&A 218, 169
Ossenkopf, V., Henning, Th., & Mathis, J.S., 1992, A&A 261, 567
Otero, S.A., & Moon, T., 2006, JAAVSO 34
Pauls, T.A., Young, J.S., Cotton, W.D., & Monnier, J.D., 2005, PASP 117, 1255
Perrin, G., Ridgway, S. T., Mennesson, B., et al., 2004, A&A 426, 279

Perrin, G., Verhoelst, T., Ridgway, S.T, et al., 2007, A&A 474, 599
Perryman, M.A.C., Lindegren, L., Kovalevsky, J., et al., 1997, A&A 323, 49
Plez, B., Brett, J.M., & Nordlund, A., 1992, A&A 256, 551
Plez, B., Smith, V.V., & Lambert, D.L., 1993, A&A 418, 812
Plez, B., van Eck, S., Jorissen, A., et al., 2003, IAUS 210, A2
Richichi, A., & Percheron, I., 2005, A&A 434, 1201
Rieke, G.H., & Lebofsky, M.J., 1985, ApJ 288, 618
Rothman, L.S., 1997, HITEMP CD-ROM (Andover: ONTAR Co.)
Rowan-Robinson, M., & Harris, S., 1982, MNRAS 200, 197
Sahai, R., 1992, A&A 253, L33
Simpson, J.P., 1991, ApJ 368, 570
Sloan, G.C., & Price, S.D., 1995, ApJ 451, 758
Sloan, G.C., & Price, S.D., 1998, ApJS 119, 141
Sloan, G.C., Kraemer, K.E., Price, S.D., & Shipman, R.F., 2003, ApJS 147, 379
Smith, V.V., & Lambert, D.L., 1985, ApJ 294, 326
Smith, V.V., & Lambert, D.L., 1986, ApJ 311, 843
Smith, B.J., 2003, AJ 126, 935
Sopka, R.J., Hildebrand, R., Jaffe, D.T., et al., 1985, ApJ 294, 242
Stencel, R.E., Nuth, J.A., Little-Marenin, I.R., & Little, S.J., 1990, ApJ 350, 45
Thomas, J.A., Robinson, G., & Hyland, A.R., 1976, MNRAS 174, 711
Tipping, R.H., & Chackerian, C. Jr., 1981, J. Mol. Spectros., 88, 352
Tsuji, T., Ohnaka, K., Aoki, W., & Yamamura, I., 1997, A&A 320, L1
Tsuji, T., 2000, ApJ 540, L99
Van Belle G.T., Dyck, H.M., Thompson, R.R., et al., 1997, AJ 114, 215
Van Belle G.T., Lane, B.F., Thompson, R.R., et al., 1999, AJ 117, 521
Van Belle G.T., & Van Belle G., 2005, PASP 117, 1263
van der Veen, W.E.C.J., Waters, L.B.F.M., Trams, N.R., & Matthews, H.E., 1994, A&A 285, 551
Van Eck, S., Jorissen, A., Udry, S., et al., 1998, A&A 329, 971
Van Eck, S., & Jorissen, A., 2000a, A&A 360, 196
Van Eck, S., Jorissen, A., & Udry, S., et al., 2000b, A&AS 145, 51
Vanture, A.D., & Wallerstein, G., 2002, ApJ 564, 395
Verhoelst, T., Decin, L., van Malderen, R., et al., 2006, A&A 447, 311
Volk, K., & Cohen, M., 1989, AJ 98, 931
Waelkens, C., Van Winckel, H., Waters, L.B.F.M., & Bakker, E.J., 1996, A&A 314, L17
Weiner, J., Danchi, W.C., Hale, D.D.S., et al., 2000, ApJ 544, 1097
Weiner, J., Hale, D.D.S., & Townes, C.H., 2003a, ApJ 588, 1064
Weiner, J., Hale, D.D.S., & Townes, C.H., 2003b, ApJ 589, 976
Weiner, J., 2004, ApJ 611, L37
Weintraub, D.A., Sandell, G., & Duncan, W.D., 1989, ApJ 340, 69
Whitelock, P., Marang, F., & Feast, M., 2000, MNRAS 319, 728
Yamamura, I., de Jong, T., & Cami, J., 1999, A&A 348, L55
Young, K., Phillips, T.G., & Knapp, G.R., 1993, ApJ 409, 725

Appendix A: Angular diameter of the calibrator β Gruis

The calibrator star β Gruis is a cool giant of spectral type M5III without any detected circumstellar matter (Sloan & Price, 1998). With an estimated angular diameter around 27 mas (Bedding et al., 1994; Heras et al., 2002), this star clearly cannot be considered as an unresolved object for the baselines used in this study.

To determine the theoretical visibility of β Gruis, one can consider this star as having a uniform disk intensity. Such a hypothesis is valid in the mid-IR because of the vanishing limb-darkening coefficient at these wavelengths. At 10 μm, the ratio between the limb-darkened angular diameter and the uniform disk angular diameter is very close to one (Davis et al., 2000). The visibility of the uniform disk is

$$V_{\rm UD}\left(\frac{B_{\rm p}}{\lambda}\right) = 2\left|\frac{J_1\left(\pi\Phi_{\rm cal}\frac{B_{\rm p}}{\lambda}\right)}{\pi\Phi_{\rm cal}\frac{B_{\rm p}}{\lambda}}\right|, \quad \text{(A.1)}$$

where $\Phi_{\rm cal}$ is the angular diameter of the calibrator β Gruis, $B_{\rm p}$ the projected baseline, λ the observing wavelength, and J_1 the first-order Bessel function of the first kind.

Previous spectrometric (Heras et al., 2002) and interferometric (Bedding et al., 1994) studies of this star allowed angular diameters of 28.1 mas and 27.0 mas, respectively, to be derived, although these evaluations bear an uncertainty of $\pm$3 mas. This corresponds to an error bar on the equivalent uniform disk visibilities reaching 20% at high spatial frequencies. Moreover, this error comes on top of the transfer function error bar of 10% (see Sect. 2). Using the observed angular diameters of β Gruis would thus carry an uncomfortably large error bar of about 30%. We therefore chose instead to predict the diameter of β Gruis by other means to reduce this error. Two methods are considered in the following, one with a dedicated SED and the other a visibility model of the star.

A.1. Spectrometric estimation

A fit of a spectral energy distribution (SED) model to the spectrometric measurements of the calibrator allows the angular diameter of the calibrator β Gruis to be determined:

$$\pi \times \left(\frac{\Phi_{\rm cal}}{2}\right)^2 I_\lambda^{\rm cal} = F_\lambda^{\rm cal}, \quad \text{(A.2)}$$

where $\Phi_{\rm cal}$ is the angular diameter of the calibrator, $I_\lambda^{\rm cal}$ the intensity of the calibrator from a MARCS model, and $F_\lambda^{\rm cal}$ the ISO/SWS spectrometric data flux of the calibrator β Gruis.

We used the MARCS code (Gustafsson et al., 1975; Plez et al., 1992, 1993), which generates stellar atmospheres of cool evolved stars, solving radiative transfer in a hydrostatic LTE environment using spherical geometry. To deduce the closest MARCS model for the calibrator β Gruis, we must know the stellar atmospheric parameters. These parameters have been derived by Judge (1986) using high-resolution spectra from the *International Ultraviolet Explorer (IUE)* satellite:

- $T_{\rm eff}$=3400$\pm$100K

– log g=0.4
– [Fe/H]=0.0.

The last stellar atmospheric parameter is the C/O ratio. The carbon abundance ($\log\epsilon(^{12}\mathrm{C})$=8.4) is scaled to the hydrogen ($\log\epsilon(\mathrm{H})$=12) and oxygen ($\log\epsilon(^{16}\mathrm{O})$=8.73) average abundances for the sample of normal M giants derived by Smith & Lambert (1985). These lead to a C/O ratio of 0.47 for β Gruis.

The U/B/V/R/I/K/L/M/[11]/[22]/[60] photometric data are taken from Johnson et al. (1966); Feinstein (1966); Mendoza (1969); Engelke (1992). Dereddening is not necessary, since the galactic latitude of the star (-58°) leads to zero visual extinction (Chen et al., 1998). Errors on the angular diameter of the star can be estimated from the phases of the 2.36-45.39 μm spectrometric data from the ISO/SWS (Infrared Space Observatory, Short-Wavelength Spectrometer) (Sloan et al., 2003). The spectra of this star were obtained on 1996 Apr 9 and 1997 May 7. Assuming a period of 37 days for the SRb variable with a V amplitude of 0.34 mag, and using the ephemeris of Otero & Moon (2006), we find that the ISO observations are taken at phases 0.61 (i.e. shortly after the photometric maximum) and 0.99, at the photometric minimum. Thus, the MIDI phases of this star are approximately intermediate between the two ISO/SWS phases, except for the 2006 June 19 observation corresponding to phase 0.01 (see Table 1).

Figure A.1 presents the best fits of the MARCS model spectrum on each of the two ISO/SWS spectrometric observations (1996 Apr 9: Phase 0.61 and 1997 May 7: Phase 0.99) yielding, from Eq. A.2, the angular diameter of the calibrator. Both fits give an angular diameter of 28.0 mas for Phase 0.61 and 25.5 mas for Phase 0.99, leading to a mean angular diameter of 26.8 mas with a mean standard deviation of 1.3 mas. This error is about 2 times smaller than the one found in the literature (Heras et al., 2002) for β Gruis, thus reducing the corresponding error bar on the uniform disk visibility (from 0.6% at low spatial frequencies to 10% at high spatial frequencies).

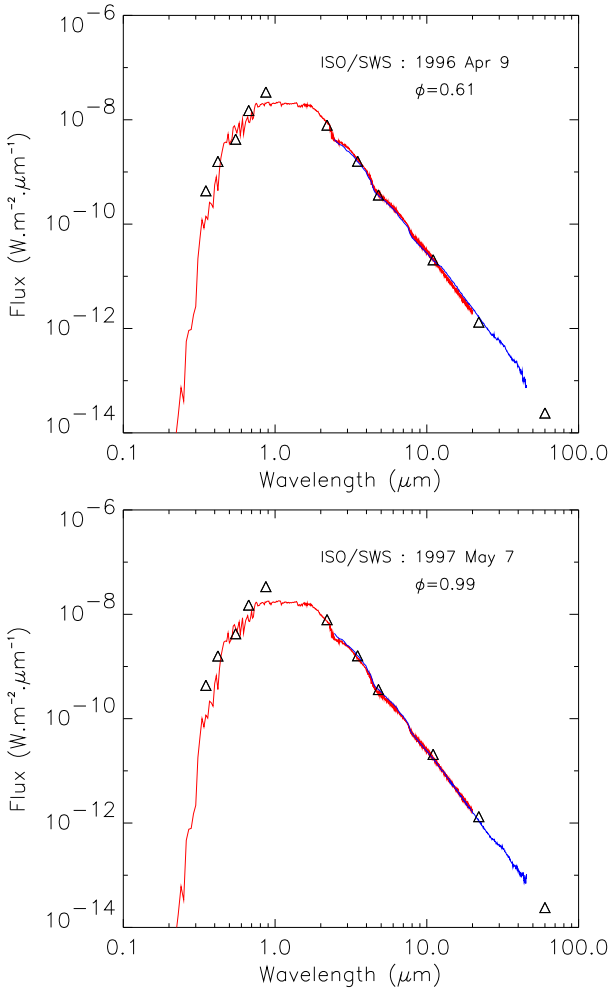

Fig. A.1. Top: best fit of the MARCS model spectrum (red line) on the calibrator β Gruis ISO/SWS data (blue line) obtained on 1996 Apr 9 (Phase 0.61). Bottom: same as the previous one for 1997 May 7 (Phase 0.99). The photometric (U/B/V/R/I/K/L/M/[11]/[22]/[60]) data of β Gruis (open triangles) are superimposed on each figure.

A.2. Interferometric estimation

Another method for deriving the angular diameter of the calibrator β Gruis consists of using observations of several calibrators observed during the same nights but at a different sky position. The journal of observations for these stars (see Table A.1) shows their spectral type and their angular diameter with their errors calculated from the ESO VLTI Calibrators Program (Richichi & Percheron, 2005), with the position, UT time, and the relative projected baselines of the calibrated sources compared to the ones for β Gruis of each observation.

This information illustrates the two main difficulties of these data. First, the time interval between the observation of β Gruis and its calibrator is rather long (from 1h30 to 4h30) in comparison to the mean intermediate time dedicated to the observation of an interferometric calibrator star. The second difficulty concerns the difference in the sky position of these calibrators compared to that of β Gruis. The differences in position are rather large (from 1 to 4h30 for the right ascension and from 10 to 55° for the declination), which may also lead to markedly different atmospheric conditions between the source and calibration observations. Consequently, the same difficulties that affect the determination of the calibrated visibility of π^1 Gruis affect the use of unresolved stars located at some distance on the sky for calibration. However, the atmospheric condition differences introduce only an amplitude bias on the calibrated visibility of the star (see Sect. 2.1),

$$V_{\mathrm{sou}} = \frac{\widetilde{V}_{\mathrm{sou}}}{\alpha\widetilde{V}_{\mathrm{cal}}}, \tag{A.3}$$

where α is a factor related to the atmospheric condition differences between the source and the calibrator observations. In the case of a simple uniform-disk intensity distribution like β Gruis, the equivalent angular diameter is independent of the α factor. This is not the case for more complex models that describe a source like π^1 Gruis, which is surrounded by a circumstellar envelope. Such models use parameters related to the α factor, which can lead to incorrect interpretation of the visibility measurements.

Figure A.2 shows the fits of the equivalent uniform disks to the calibrated spectrally-dispersed visibilities of β Gruis

Table A.1. Journal of observations of the calibrators observed the same nights as β Gruis.

Star	Spectral type	Right ascension ; Declination	UT date & Time	d_{UD}[mas]	Base[m]	PA[deg]
β Gru	M5III	22 42 40 ; -46 53 04	2006-05-25 07:51:28	...	60.2	32
ϵ Peg	K2Ib	21 44 11 ; +09 52 30	2006-05-25 09:24:17	7.7±0.2	59.1	75
β Gru	M5III	22 42 40 ; -46 53 04	2006-05-25 07:51:28	...	60.2	32
η Sgr	M3.5III	18 17 38 ; -36 45 42	2006-05-25 03:25:52	11.9±2.1	56.2	34
β Gru	M5III	22 42 40 ; -46 53 04	2006-08-08 08:13:56	...	57.2	93
τ^4 Eri	M3/M4III	03 19 31 ; -21 45 28	2006-08-08 10:09:22	10.6±1	62.9	66

calculated from each of the 3 calibrators (see Table A.1). The calibrated visibilities were derived with the MIA and EWS packages and exhibit very good agreement between the data sets. The error bars on the calibrated visibilities are typically between 10 and 15%. The mean of the equivalent diameters of the 3 fits is 28.8 and the corresponding error is 0.6 mas.

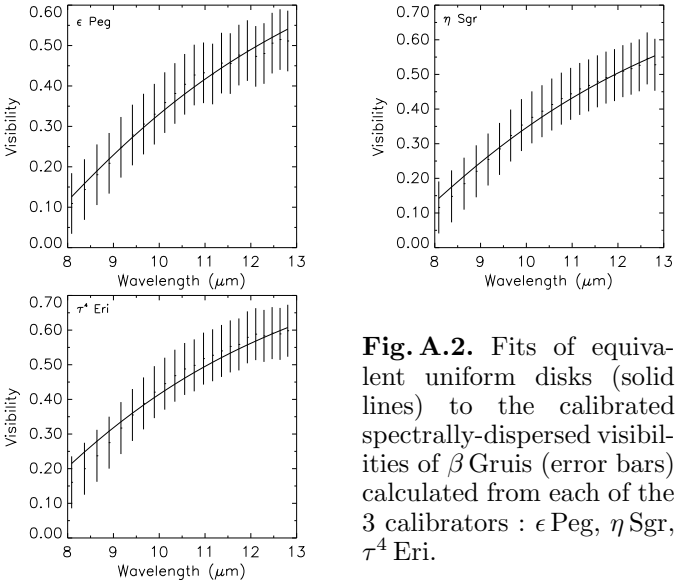

Fig. A.2. Fits of equivalent uniform disks (solid lines) to the calibrated spectrally-dispersed visibilities of β Gruis (error bars) calculated from each of the 3 calibrators : ϵ Peg, η Sgr, τ^4 Eri.

Table A.2 lists the angular diameters of β Gruis found in the literature and those derived in this paper using the spectrometric and interferometric methods.

Table A.2. Determination of the angular diameter (in mas) of β Gruis with different methods.

Reference	Value (mas)
Heras et al. (2002)	28.11±2.82
Bedding et al. (1994)	27±3
Spectrometric method (this work)	26.8±1.3
Interferometric method (this work)	28.8±0.6

Diameters determined from these last two methods will be taken into account to reduce calibrated visibilities of π^1 Gruis. The best set of calibrated visibility data will then be the one giving the most reliable parameter values, for which we will be able to simultaneously fit the source spectrum and visibilities.

List of Objects

'π^1 Gruis' on page 1
'π^1 Gruis' on page 1
'β Gruis' on page 1
'π^1 Gruis' on page 1
'π^1 Gruis' on page 1
'Hen 4-202' on page 1
'HD 212087' on page 1
'HIP 110478' on page 1
'R And' on page 1
'R Cyg' on page 1
'π^1 Gruis' on page 1
'π^1 Gruis' on page 1
'π^1 Gruis' on page 2
'π^1 Gruis' on page 2
'π^1 Gruis' on page 2
'V Hya' on page 2
'π^1 Gruis' on page 2
'π^1 Gruis' on page 2
'π^1 Gruis' on page 2
'β Gruis' on page 2
'π^1 Gruis' on page 2
'β Gruis' on page 2
'π^1 Gruis' on page 3
'β Gruis' on page 3
'π^1 Gruis' on page 3
'β Gruis' on page 3
'π^1 Gruis' on page 3
'β Gruis' on page 3
'π^1 Gruis' on page 3
'β Gruis' on page 3
'π^1 Gruis' on page 3
'β Gruis' on page 3
'π^1 Gruis' on page 3
'β Gruis' on page 3
'π^1 Gruis' on page 3
'β Gruis' on page 3
'β Gruis' on page 3
'π^1 Gruis' on page 3
'π^1 Gruis' on page 3
'π^1 Gruis' on page 3
'π^1 Gruis' on page 3
'π^1 Gruis' on page 3
'π^1 Gruis' on page 3
'β Gruis' on page 3

‘π^1 Gruis’ on page 3
‘π^1 Gruis’ on page 3
‘β Gruis’ on page 3
‘β Gruis’ on page 3
‘β Gruis’ on page 3
‘π^1 Gruis’ on page 4
‘π^1 Gruis’ on page 4
‘π^1 Gruis’ on page 4
‘π^1 Gruis’ on page 4
‘π^1 Gruis’ on page 4
‘π^1 Gruis’ on page 5
‘π^1 Gruis’ on page 5
‘π^1 Gruis’ on page 5
‘π^1 Gruis’ on page 5
‘π^1 Gruis’ on page 5
‘π^1 Gruis’ on page 5
‘π^1 Gruis’ on page 5
‘π^1 Gruis’ on page 5
‘π^1 Gruis’ on page 5
‘π^1 Gruis’ on page 5
‘π^1 Gruis’ on page 6
‘π^1 Gruis’ on page 6
‘π^1 Gruis’ on page 6
‘π^1 Gruis’ on page 6
‘π^1 Gruis’ on page 6
‘π^1 Gruis’ on page 7
‘π^1 Gruis’ on page 7
‘β Gruis’ on page 7
‘β Gruis’ on page 7
‘π^1 Gruis’ on page 7
‘π^1 Gruis’ on page 7
‘π^1 Gruis’ on page 7
‘π^1 Gruis’ on page 7
‘π^1 Gruis’ on page 7
‘π^1 Gruis’ on page 8
‘π^1 Gruis’ on page 8
‘π^1 Gruis’ on page 8
‘π^1 Gruis’ on page 8
‘π^1 Gruis’ on page 8
‘π^1 Gruis’ on page 9
‘π^1 Gruis’ on page 9
‘π^1 Gruis’ on page 9
‘π^1 Gruis’ on page 9
‘π^1 Gruis’ on page 9
‘π^1 Gruis’ on page 10
‘π^1 Gruis’ on page 10
‘π^1 Gruis’ on page 11
‘π^1 Gruis’ on page 11
‘π^1 Gruis’ on page 11
‘V Hya’ on page 11
‘π^1 Gruis’ on page 11
‘π^1 Gruis’ on page 11
‘π^1 Gruis’ on page 12
‘π^1 Gruis’ on page 12
‘π^1 Gruis’ on page 12
‘π^1 Gruis’ on page 12
‘π^1 Gruis’ on page 12
‘π^1 Gruis’ on page 12
‘π^1 Gruis’ on page 13
‘π^1 Gruis’ on page 13
‘π^1 Gruis’ on page 13
‘π^1 Gruis’ on page 13
‘β Gruis’ on page 14
‘β Gruis’ on page 14
‘β Gruis’ on page 14
‘β Gruis’ on page 14
‘β Gruis’ on page 14
‘β Gruis’ on page 14
‘β Gruis’ on page 14
‘β Gruis’ on page 14
‘β Gruis’ on page 14
‘β Gruis’ on page 15
‘β Gruis’ on page 15
‘β Gruis’ on page 15
‘β Gruis’ on page 15
‘β Gruis’ on page 15
‘β Gruis’ on page 15
‘β Gruis’ on page 15
‘β Gruis’ on page 15
‘π^1 Gruis’ on page 15
‘β Gruis’ on page 15
‘π^1 Gruis’ on page 15
‘β Gruis’ on page 15
‘β Gruis’ on page 16
‘β Gru’ on page 16
‘ϵ Peg’ on page 16
‘β Gru’ on page 16
‘η Sgr’ on page 16
‘β Gru’ on page 16
‘τ^4 Eri’ on page 16
‘β Gruis’ on page 16
‘ϵ Peg’ on page 16
‘η Sgr’ on page 16
‘τ^4 Eri’ on page 16
‘β Gruis’ on page 16
‘β Gruis’ on page 16
‘π^1 Gruis’ on page 16